BAMS Article

Fireworks on Weather Radar and Camera

D. S. Zrnić, P. Zhang, V. Melnikov, and E. Kabela

ABSTRACT: High-sensitivity weather radars easily detect nonmeteorological phenomena characterized by weak radar returns. Fireworks are the example presented here. To understand radar observations, an experiment was conducted in which the National Severe Storms Laboratory (NSSL)'s research (3-cm wavelength) dual-polarization radar and a video camera were located at 1 km from fireworks in Norman, Oklahoma. The fireworks from the 4 July 2017 celebration were recorded by both instruments. The experiment is described. Few bursts recorded by the camera are analyzed to obtain the height of the explosion, its maximum diameter, number of stars, and the duration of the visible image. Radar volume scans are examined to characterize the height of the observation, the maximum reflectivity, and its distribution with height. The fireworks location is close to the Terminal Doppler Weather Radar (TDWR) that operates in single polarization at a 5-cm wavelength and monitors hazardous weather over the Oklahoma City airport. A third radar with data from the event is the Weather Surveillance Radar-1988 Doppler (WSR-88D) located in Norman. It has a wavelength of 10 cm and supports technical developments at the Radar Operation Center. Reflectivity factors measured by the three radars are compared to infer the size of dominant scatterers. The polarimetric characteristics of fireworks returns are analyzed. Although these differ from those of precipitation, they are indistinguishable from insect returns. Radar observation of larger fireworks in Fort Worth, Texas, with a WSR-88D is included and compared with the observations of the smaller fireworks in Norman. We expect the detectability of explosions would be similar as of fireworks. Pinpointing locations would be useful to first responders, or air quality forecasters. A benefit of fireworks recognition in weather radar data is that it can prevent contamination of precipitation accumulations.

AFFILIATIONS: **Zrnić**—National Severe Storms Laboratory, Norman, Oklahoma; **Zhang, Melnikov**—Cooperative Institute for Mesoscale Meteorological Studies, University of Oklahoma, Norman, Oklahoma; **Kabela**—Oak Ridge National Laboratory, Oak Ridge, Tennessee

https://doi.org/10.1175/BAMS-D-18-0248.1

Corresponding author: Dušan Zrnić, dusan.zrnic@noaa.gov

In final form 16 October 2019

The primary mission of weather radars is to locate storms, detect hazards within, and quantify the amounts of precipitation. This justified the upgrade of the Weather Surveillance Radar-1988 Doppler (WSR-88D) network to dual polarization (Zrnić 2003) that added new capabilities to operational weather radars: namely, identification of different scatterer types (Park et al. 2009), further improvement in QPE (Ryzhkov et al. 2014), and potent depiction of storm features (Hubbert et al. 2018; Ryzhkov and Zrnić 2019).

Besides serving these main missions, applications broadened to satisfy different objectives than those initially intended. Radars have become indispensable tools in the arsenal of aeroecologists (Chilson et al. 2012). Particularly useful is discrimination between insects and birds (Stepanian et al. 2016) made possible by dual polarization (Zrnić and Ryzhkov 1998). Identification of volcanic ash (Marzano et al. 2013) and tornadic debris (Ryzhkov et al. 2005) are other auxiliary benefits from weather radars.

High sensitivity of these radars enables detection and tracking of smoke plumes caused by forest fires (Banta et al. 1992) and support management of wildfires (Hufford et al. 1998). Especially beneficial is better than 5 min average delay in detection of the fire onset compared to the 15 min delay considered the low limit for good conventional systems (Saraiva et al. 2014). Melnikov et al. (2008) document polarimetric characteristics of grass fires and display reflectivities up to 20 dBZ. Rogers and Brown (1997) describe in detail radar observations of an industrial fire in Montreal, Canada. They present simultaneous observations with a vertically pointing 3-cm wavelength radar and a 33-cm wavelength wind profiler. The reflectivities measured with the profiler reach 40 dBZ. The reflectivities at 3-cm wavelength are about 20 dB lower. The authors offer two explanations. One is that the particles of about 1 cm are Mie scatterers at the 3-cm wavelength but are still Rayleigh scatterers at the 33-cm wavelength and reflect significantly larger power (see "Backscattering, Rayleigh and Mie regime" sidebar). The other is that backscattering by refractive index fluctuations caused by intense flame enhances the returns at the longer wavelength. Erkelens et al. (1999) hypothesize that coherent scattering from variation of particle distribution in range may be the strong contributor to the reflectivity at the 33-cm wavelength.

Users expect that the capabilities of the WSR-88D will remain in any future replacement technology. One candidate is the multifunction phase array radar (Weber et al. 2007; Zrnić et al. 2007). Besides serving weather and aviation

Backscattering, Rayleigh and Mie regime

The size, composition, and orientation of stars or other scatterers determines the values of the backscattered polarimetric variables at different radar wavelengths. As an electromagnetic wave impinges on a scatterer two things happen. It is reflected by the scatterers surface closest to the radar, and it also penetrates the scatterer and sets internal reflections within the scatter's shell. At each internal reflection, part of the wave leaves the scatterer in the direction of the radar. This wave interacts with the primary reflected wave and, if scatterers are small compared to the wavelength, the two add almost in phase. Then the reflectivity factor increases in proportion to the sixth power of size (diameter) and the process is referred to as Rayleigh scattering. For oriented oblate Rayleigh scatterers such as raindrops, the differential reflectivity (ratio of H to V returned power in log units) at the 10 cm wavelength increases monotonically with size.

The H and V signals received by radar differ in phase. Their phase difference Φ_{DP} consists of system differential phase Φ_{DP}(system), propagation differential phase Φ_{DP}(propagation), and backscatter differential phase δ. Φ_{DP}(propagation) is caused by cumulative accumulation of phase difference through propagation in oriented hydrometeors between the antenna and the location of sampled backscatterers. Insects' contribution to Φ_{DP}(propagation) is negligible and so is their contribution to δ (provided they are Rayleigh scatterers).

Mie scatterers are larger than the Rayleigh ones. For these, the two superposing waves (one reflected from the outside front surface of the scatterer the other from the back inside surface) can add constructively or destructively depending on size and this causes the reflectivity to oscillate as the size increases. If the scatterer is nonspherical but oriented so that its larger (or smaller) axis is aligned with horizontally polarized field, the oscillations of reflectivity at horizontal and vertical polarization are not in sync. Depending on size, either reflectivity can be larger, and therefore the differential reflectivity can be positive or negative. Similarly, the backscatter differential phase δ can have a large positive or negative value.

needs, such radar could enhance homeland security by detecting noncooperative flying threats and ground-based explosions. Both malicious and accidental explosions can release harmful chemicals, and weather radar may track these. Even in cases where the plume's reflectivity is too weak for tracking, locating the initial explosion may be sufficient to provide, via numerical models, downwind conditions and warn the public of impending hazards. Use of fireworks is a reasonable test for detection and tracking of explosions and plumes (see "Fireworks" sidebar).

Observations of Norman, Oklahoma, municipal fireworks from multiple weather surveillance radars and high-speed photography are analyzed. The fireworks were captured from close range with an experimental dual-polarization 3-cm wavelength radar and high-speed camera. Additional data from a nearby Terminal Doppler Weather Radar (TDWR) (5-cm wavelength) and WSR-88D (10-cm wavelength) are used for comparison of firework characteristics. The Norman fireworks have smaller caliber shells than fireworks in major cities. Therefore, fireworks from Fort Worth, Texas, observed by a nearby WSR-88D are presented for additional comparison. Our quantitative analysis considers the fireworks as rigid scatterers. Nonetheless, we make inferences concerning contribution by refractivity.

Experimental setup

Data from the Norman fireworks launched at Reeves Park on 4 July 2017 were observed by three weather radars: the Oklahoma City, Oklahoma, TDWR (code designation TOKC; the radar is located in Norman), the WSR-88D (code designation KCRI) in Norman, and the National Severe Storms Laboratory (NSSL) X-band Experimental Radar for Environmental Studies (XERES). Figure 1 shows the location and distance of each radar from the firework launch site. The radars' specifications are in Table 1 and Fig. 2 displays the XERES mobile setup.

We placed XERES close to the launch site (Fig. 3) and the Panasonic HC-VX981 video camera next to it. The camera has 1,920 × 1,080 image resolution and records 23.98 frames per second. From the images and the map, we established distances between launch site and the size of the beam cross section of each radar (Fig. 4). The images also capture the height, evolution, and duration of individual bursts.

During the approximately 15 min fireworks show, XERES scanned a 35° wide sector starting from 343° (where north is 0°) to 18°. It takes 7 s to scan through this sector at a single elevation angle. Multiple elevation sweeps from 2° to 10° in increments of 1° were collected to make a volume of data. It took one minute to complete the volume scan so we had approximately 15 volumes of fireworks data.

Fireworks

There are many types of fireworks. Most are shot by mortar or rocket propelled (Siegel 2016). The shell is a paper enclosure filled with pellets called stars, usually cylinders, cubes, or spheres. In the shell's core is the burst powder. It is ignited by a time fuse set to activate at the apogee, after which the explosion ignites the stars, expelling them in different directions. Spherical shells are often filled with spherical stars and burst in almost perfect symmetry, creating spherical patterns in the sky. Peony shells burst into stars that do not leave trails. A spherical burst in which the stars leave a continuous trail is called chrysanthemum. Various metals and oxidizing agents in the stars produce desirable colors. The shells come in various shapes and sizes, typically from 2 to 16 in. At grand spectacles the shell can be 2 to 3 ft in diameter. The larger ones reach greater heights and produce wider displays. In the Norman fireworks, the largest diameter of the shells was 8 in., and these can reach about 250 m in height and burst to about 110 m. A great variety of shells and stars is used at the same celebration and often simultaneously. The diverse shapes and sizes of stars and their composition directly impact the reflection of electromagnetic waves and therefore the polarimetric variables. We observed during the Norman event that displays of several fireworks overlap in time. That is a reason why it is very hard to associate an individual firework with its radar observation. In cases where there is a time gap between bursts, it is possible to associate a radar scan with a time period in which the burst occurred. But, the synchronization of timing within the burst and the specific radial position are too coarse to establish the spatial relation between the radar observation and the state of the burst. Nonetheless, analysis of individual video images can help physical explanations and set some bounds on radar measurements.

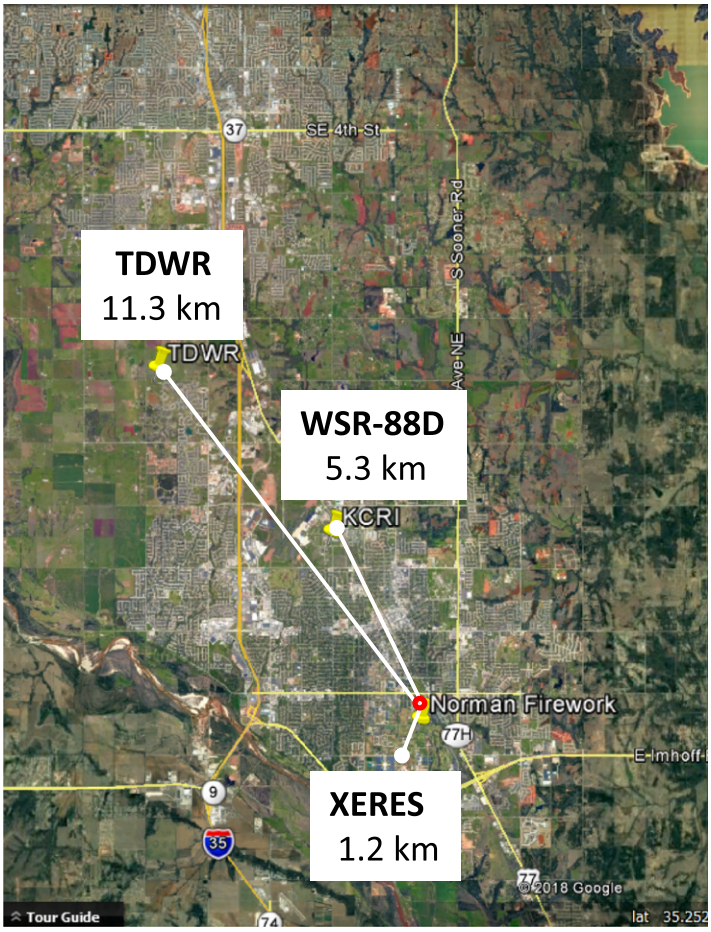

Fig. 1. Locations of the Terminal Doppler Weather Radar (5.35-cm wavelength) serving the Oklahoma City Airport, the WSR-88D (10-cm wavelength) in Norman supporting the network of National Weather Service radars, the XERES research mobile radar (3.2-cm wavelength), and the fireworks (red circle). The ranges from the radars to the fireworks location are indicated. The image is from Google Earth.

Fig. 2. The 3.2-cm wavelength mobile research radar, XERES. The antenna is an exact scaled down version of the antenna on the WSR-88D.

Table 1. Radar parameters.

Parameter	XERES (NOXP)	TDWR (TOKC)	WSR-88D (KCRI)
Wavelength (cm)	3.2	5.35	10
Beamwidth (°)	1	0.55	1
Pulse width (ms, m)	0.5, 75	1.1, 165	1.57, 235
Sample spacing in range (m)	75	150	250
Spacing of radials in azimuth (°)	1	1	0.5
Scan	Sector	PPI	PPI
Volume update (min)	1	6	4

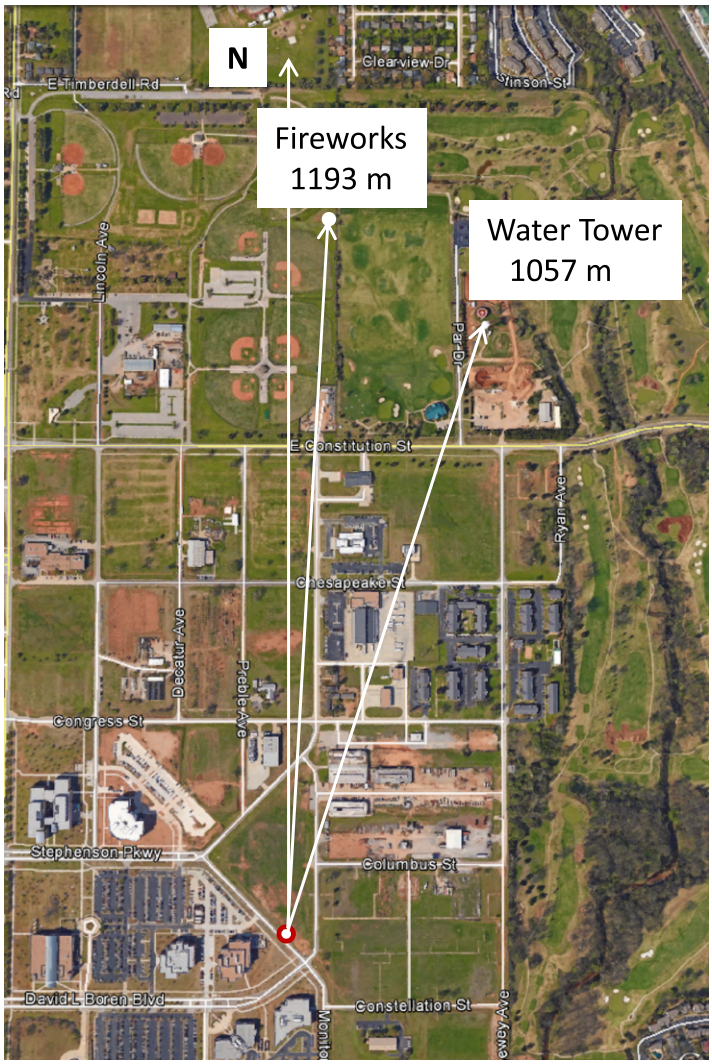

Fig. 3. Location of the fireworks launch site and XERES (3.2-cm wavelength) mobile radar (red circle at the bottom) on the University of Oklahoma campus. The distances of the launch site and the water tower from the radar are indicated and the radar azimuth of the tower is 16.48°. The satellite image is from Google Earth.

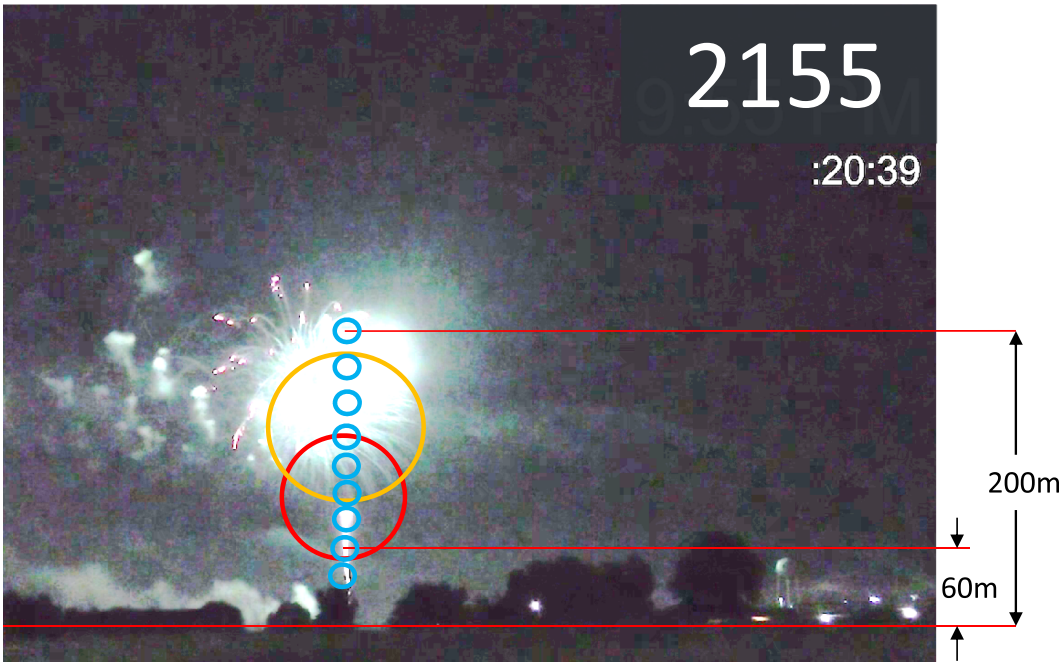

Fig. 4. View of fireworks in Reeves Park, Norman, from the location of the XERES. The water tower on the right is the same one as in Fig. 3. The circles depict radar beam cross sections. The centers of the beam cross sections of the XERES radar are at the heights of its elevation scans and the cross sections (blue circles) are in the plane of the image. The cross sections of the other radar beams are for their lowest elevation (0.5°) scans and cut the image plane but are plotted in it for reference. The circle colors refer to radars as follows: XERES (blue), WSR-88D (red), TDWR (yellow). The indicated heights are above ground level (AGL) at the fireworks location. The bottom red line marks the ground level at the launch site, which happens to be the same as the ground level at the XERES location. The time at the top right is CDT hours and minutes. The time below it relates to the seconds and hundredths of seconds for this snapshot.

Visual observations

The images in Fig. 5 depict time evolution of an average peony firework. Immediately after explosion its visible burning segments, called "stars" by the American Pyrotechnics Association, are on a spherical surface expanding uniformly because the effect of gravity is negligible compared to the drag force (proportional to the square of velocity) slowing the expansion. From these images we estimated the velocity of the radial expansion $v(t)$ by tracking a star (Fig. 6) propelled in the horizontal direction. Invoking Newton's second law, we obtain the model velocity

$$v(t) = \frac{v_o}{1 + \rho c_d A v_o t / (2M)}, \qquad (1)$$

where v_o is the initial (impulse) expansion velocity (m s^{-1}) at time 0, c_d is the drag coefficient, M is the star mass (g), ρ is air density (g m^{-3}), and A is the effective area (m^2) of the star perpendicular to its velocity. We ignored the mass lost from burning, which at the beginning is small but increases with time and further slows the star, as seen in the last couple of data points (Fig. 6). To check physical adequacy of this model, we computed the drag coefficient from the parameters of the fitted curve (listed in the caption of Fig. 6). This required further assumptions, including a spherical star 1-cm in diameter, which is common for shells 8 in. in size (Shimizu 2006). The largest shells in Norman were 8 in. (reported by the Norman Parks and Recreation Department). So for a 1-cm star $A = 0.25\pi\ 10^{-4}$ m^2 (i.e., 0.25 π cm^2). The stars' density (see the appendix) is 0.9 g cm^{-3} and the air density is 0.00112 g cm^{-3} at 330 m above sea level. After conversion to the mks units and computing the mass M, we equate $\rho c_d A/(2M)$ to 0.04, which is the coefficient in the fitted curve listed in the caption of Fig. 6. From that equality $c_d = 0.43$, which is in the range 0.1 to 0.5 of values for smooth spheres with Reynolds numbers 10^5 to 10^6.

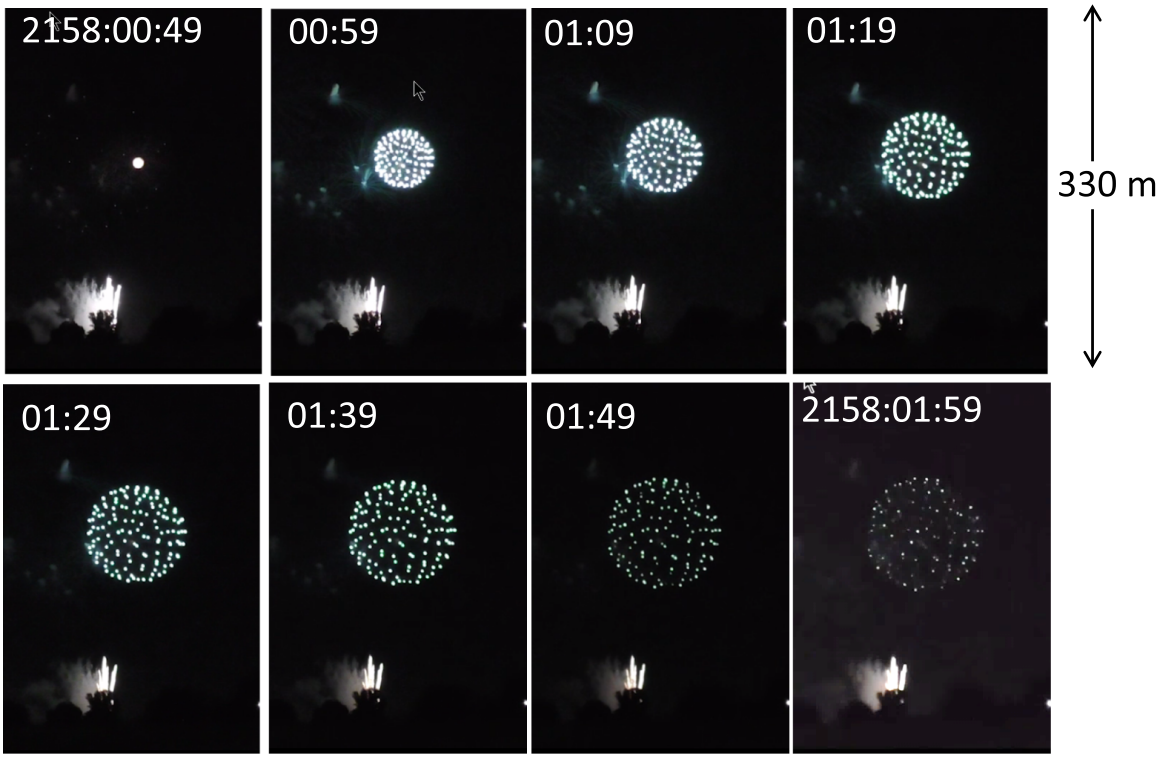

Fig. 5. Time sequence of a burst in 0.1 s intervals starting at 2158:00:49 CDT. The first and second digits in the last pair of the time stamp are tenth and hundredth of a second.

The illumination lifetime of this burst is about 1 s; time zero (Fig. 6) starts between 0.02 and 0.04 s after the burst onset when individual stars became identifiable. The proportionality of drag force to the square of velocity is an adequate model for the initial motion of the star. The largest diameter of this burst is about 100 m and the number of stars we counted is 121. The height of explosion is 190 m above ground. Many similar fireworks were part of the show. Concerning the star size, 12 mm according to Shimizu (2006), is at the small end of sizes in commercial fireworks. The largest diameters are over 18 mm. The size of stars, their dielectric constant, and the radar wavelength determine whether the stars would backscatter in the Rayleigh or Mie regime (see appendix).

To determine the terminal velocity in different types of bursts we tracked, frame by frame, the descending stars on the video images. The terminal velocities of stars in peony bursts (the most frequent) are about 14 to 16 m s^{-1}. Stars stuck together fall at about 7 m s^{-1} and very few had this form. High terminal velocities of 22 m s^{-1} we estimated in a willow burst (Fig. 7) from star trajectory toward the end of visible state. Similar large values we found in bursts like the one in the upper-right corner of Fig. 7. If the stars' diameters were 1 to 4 cm, our estimated terminal velocities would be at the high end of hail terminal velocity. Plots by Heymsfield et al. (2018) show that 1 cm

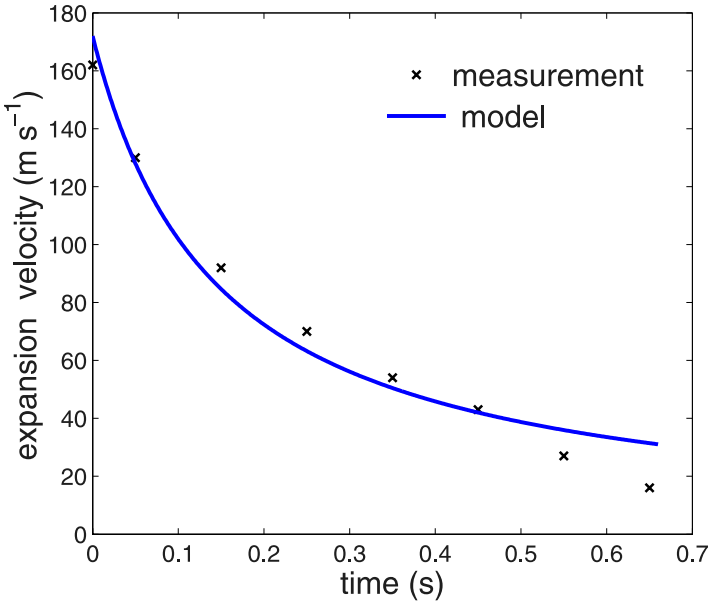

Fig. 6. Expansion velocity vs time of the burst in Fig. 5; *x* indicates estimates from images and the solid curve is the fit $v(t) = 170/(1 + 0.04 \times 170t)$ to the physical model in which drag force slows the "star."

hail's 90th percentile terminal velocity is 10 m s^{-1}, and 4 cm hail's 90th percentile is 20 m s^{-1}. The stars of similar size likely experience less drag and fall faster, as our measurements indicate. This suggests that sizes on the order of 1 cm are a reasonable estimate for Norman fireworks. They are within the 6 to 12 mm sizes of stars, which according to Shimizu's (2006) fill 3- to 8-in. shells.

Observed burst diameters are mostly between 100 and 150 m, and few exceed 200 m. Duration of the visible effects of small bursts is 1 to 2 s, and large bursts last 5 to 6 s. Many chrysanthemum fireworks were part of the show, and the recommended burning time for their stars is less than 5 s (Shimizu 2006, p. 435). The average number of bursts per minute is about 33. Of these, 88% occurred between 100 and 200 m off the ground, 8% at heights above 200 m, and 4% below 50 m.

Visual observations indicate that stars replenish quasi continuously the volume above the launch site. Fireworks are launched on average every 2 s; nonetheless, very frequently fireworks are launched in bunches so some bursts overlap in space and time. Additionally, the rockets carrying the shell may crisscross the resolution volumes. The largest number of stars we counted is 325 in a peony. Most large values are 200 to 300. In cases of overlapping bursts, the number of stars in the radar resolution volume could be 2 to 3 times more. The number and the location within the resolution volume determine the reflectivity.

Fig. 7. Front: Willow fireworks 2.3 s after burst (at 2000:16 CDT). The three smaller bursts are at earlier stage of development. The one in the upper-right corner is at 270 m above ground.

Experiment with the 3-cm wavelength radar

The fireworks appear as an increased reflectivity, Z within a small sector (150 m in azimuth and 225 in range), which is centered on the location where fireworks are launched. The position of a maximum may remain at the same location or shift. Because the separation between elevation scans is 7 s, the returns in consecutive scans in elevation are most likely from different burst. We have examined Z from consecutive scans at 1 min intervals (same azimuth and elevation). In many cases, the fireworks reflectivity of 20 dBZ is followed by the environmental value of 10 dBZ. This indicates that if the scatterers were refractivity fluctuations (on scales of 1.5 cm) their lifetime would be shorter than 1 min.

Plots of the radar variables (Fig. 8) are typical of the XERES observations. The enhanced Z in the 8° elevation scan (Fig. 8, top left, inside the white circle) is from fireworks, and the corresponding small negative Z_{DR} (Fig. 8, bottom left) is indistinguishable from similar values in the environment. The vertical (RHI) cross section of Z_{DR} exhibits a −2 to 4 dB range (Fig. 8, enclosed with the ellipse), implying presence of diverse scatterers such as stars and biota composed of insects and/or birds and bats.

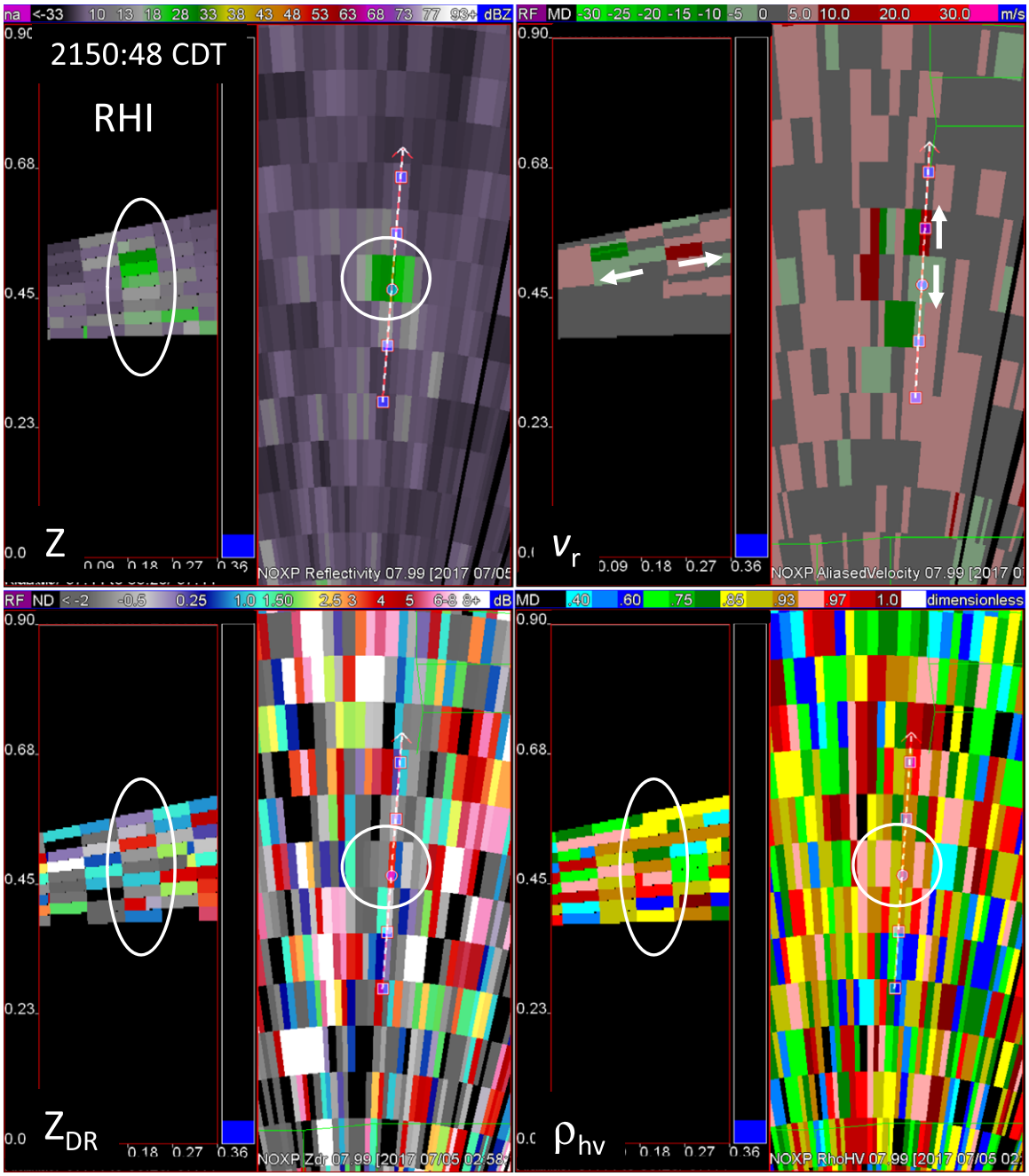

Fig. 8. XERES (3.2-cm wavelength) data. (top left) Reconstructed vertical (RHI) cross section from consecutive sector scans at different elevations starting with the first scan at 2° and conical (PPI) cross section from the scan at 8° elevation of the reflectivity, *Z* field, at 2150:48 CDT. The enhanced reflectivity of 33 dB*Z* (inside the ellipse and the circle) is from the fireworks whereas the background of less than 15 dB*Z* is mainly due to insects. The continuity in height (RHI plot; three contiguous green pixels) suggests part of the return could be from a single burst. But, the difference in time when the top and bottom radial data are collected is 14 s, which is about 3 times more than the longest duration of visible bursts. Because the average number of bursts in 15 s is about 8 it follows that different fireworks have contributed to the enhanced *Z*. (top right) As in top left, but the fields of Doppler velocity v_r are plotted. The radial divergence indicated with arrows is the only one detected by XERES. (bottom left) As in top left, but the fields of differential reflectivity Z_{DR} are plotted. (bottom right) The fields of the correlation coefficient ρ_{hv}. The color bars above the images indicate categories of reflectivity in dB*Z*, Doppler velocity in m s^{-1}, differential reflectivity in dB, and correlation coefficient values between 0 and 1. The arrow indicates the radar beam (azimuth) at which the RHI was constructed.

The ρ_{hv} field in both conical and vertical cross sections has values smaller than 0.97 almost everywhere, typical of nonmeteorological returns. At the location of the fireworks (enclosed with the circle in Fig. 8), it is closer to 0.97 (and somewhat uniform), which is the upper value for large (2.5 to 5 cm) hail (Ryzhkov and Zrnić 2019). The backscatter differential phase (δ, not shown) is close to 0° as expected from Rayleigh scatterers or spherical scatterers of any size. At other times, the variation of δ is small but different from zero (−7° to 2°), as would be from nonspherical scatterers at the low end of Mie sizes. Considering the distribution of stars within the beam may not be uniform, that biota is in the resolution volumes, and statistical errors, we conclude that some stars could be Rayleigh scatterers. In summary, none of the polarimetric variables has information for unambiguously distinguishing the fireworks from the background biota.

The field of Doppler velocities contains a couplet of radial divergence signatures in both RHI and conical cross sections (Fig. 8). This would happen if the radial extent of the sample (resolution) volume were smaller than the burst size and the burst straddles two resolution volumes; it is barely the case here because both the length of the resolution volume and sample spacing are 75 m, and the bursts' maximum size is less than about 150 m. Therefore, the stars are the main source of Z in this example as opposed to refractivity perturbations, which would not exhibit divergence because they are passive wind tracers.

The Doppler spectrum width, σ_v, quantifies the dispersion of the scatterers' velocities inside the radar resolution volume. The 6 to 7 m s^{-1} values in one scan (not presented) are the highest recorded by this radar; in all other scans values are under 1.5 m s^{-1}.

The moving burning stars create turbulent eddies along their paths. The 1.5 cm size eddies could contribute to the returns. If they were dominant, they would produce zero differential reflectivity and Doppler velocity equal the one from the environment. This, we do not observe in our data.

Observation with the other radars

Important considerations for interpreting radar observations are wavelength, size of the resolution volume, and the height of the beam center at the location of the fireworks. The lateral beam dimensions are listed in Table 2 and depicted in Fig. 4. Frequent observations such as in the monitor mode of the TWDR (Rauber and Nesbitt 2018, p. 244) are crucial for detecting the fireworks.

Scans at elevation angles of 0.5° and 1.0° by the TDWR enable capturing information from 50 to 200 m above the ground and these were used. Volume scans take 6 min; therefore, three are completed during the 15 min firework show. Because the 0.5° elevation angle is scanned twice in the monitor mode, there are six scans of 0.5° data and three scans of 1.0° data.

A peak of reflectivity appears above the location of fireworks in each of the six 0.5° elevation scans and each of the three 1° elevation scans. The increase and persistence of the signal is what distinguishes it from the reflectivities in the environment (Fig. 9). Comparison of a peak with the value at the exact same location but 20 s later is possible for all three available scan pairs. In each, the later value was smaller by 1 to 4 dB. This may be coincidental and due to the distribution of stars and their number from new bursts in these particular resolution volumes. If the principal contribution to the peaks were by refractivity fluctuations, the smaller values would indicate demise of turbulent eddies (2.5 cm size) in about 20 s. Over this short period

Table 2. Geometric factors at the location of Norman fireworks.

Radar	Beam lateral dimension	Beam center height (m)	Resolution volume
XERES	20 m	60 to 200, in steps of 20	7,500π m^3
TDWR	110 m	140 and 230	453,750π m^3
WSR-88D	90 m	90 and 135	476,890π m^3

eddies would drift with the mean wind. This we did not see either because the lifetime was shorter or the irregularities effects were negligible.

The spectrum widths are 2 to 4 m s^{-1}. These are bigger than from XERES (σ_v < 1.5 m s^{-1}). TDWR's beam center is higher and its resolution volume is 60 times larger. Therefore, the wind shear effects spread more the velocity of the star and/or refractivity fluctuations within the resolution volume.

The WSR-88D captured fireworks data in all its low elevation scans: four scans at 0.5° elevation separated in time by 3.5 min, and two at 0.9° separated by 6 min. In contrast to the TDWR observation, the reflectivity peak of fireworks (Fig. 10) is indistinguishable from similar sporadic peaks of "other scatterers." Only time persistence of enhanced reflectivity over the fireworks location and continuity in the lowest two elevations (Fig. 10) alerts that an anomaly is present. The σ_vs (not plotted) are 2 to 3 m s^{-1}, which are smaller than the 4 m s^{-1} from TDWR because WSR-88D scans are at lower altitudes and its beam cross section is 33% less than TDWR's. Similar to the measurements with XERES, the polarimetric variables of the fireworks are indistinguishable from the background. At the end of the show, there was a spectacular display of almost simultaneous bursts. The first scan of the WSR-88D after the show's end was 2 min later. It had no signals from the fireworks implying that if eddies sized 5 cm were significant contributors their lifetime would have been shorter than 2 min.

Comparisons

Next, we present the average peak reflectivities as well as the range of values measured by the three radars at different heights (Fig. 11). In the XERES data at the highest elevation (10° and beam center at 210 m), 10% fewer scans had evidence of fireworks (i.e., enhanced Z) than at the lower elevations. This could be because fewer bursts occurred at that height and these were seldom overlapping hence were missed due to the 1-min volume scan revisit time. The trend in Fig. 11 is a slight decrease of average reflectivity with height for all three radars. This may be because there were more overlapping bursts at low altitudes, increasing the number of stars in the radar resolution volume and consequently reflectivity.

Let us examine the stars' concentration and sizes, and

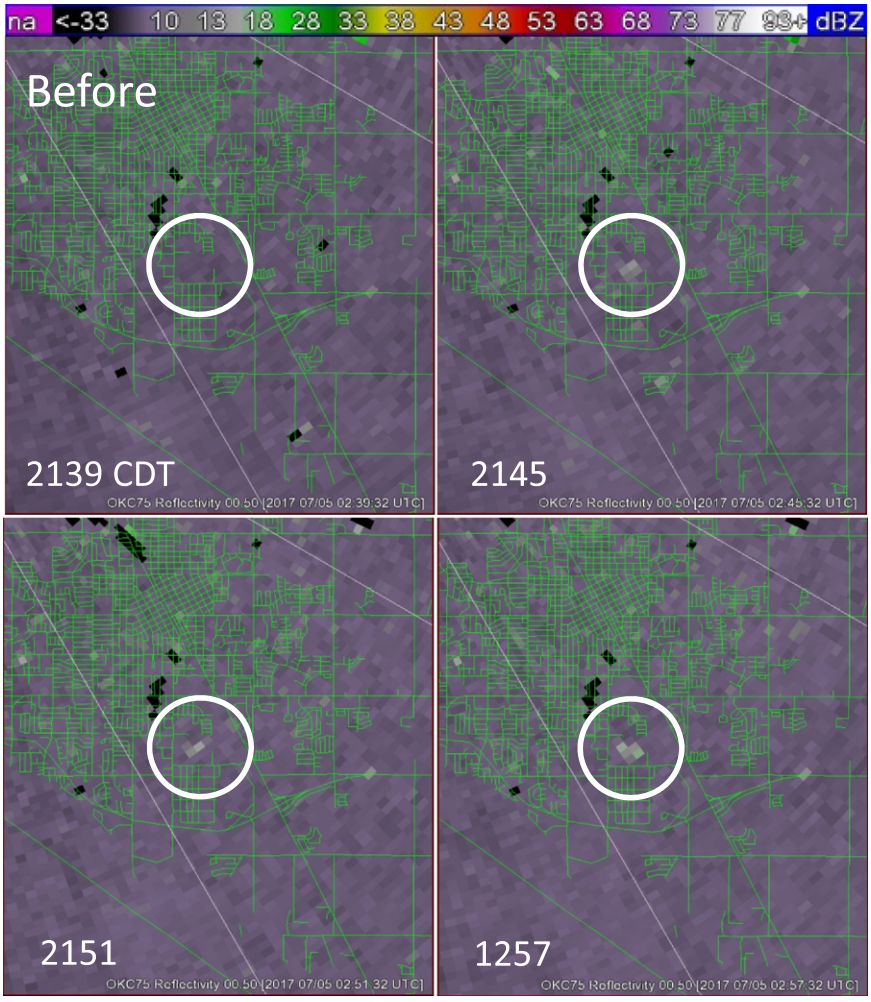

Fig. 9. Reflectivity fields of fireworks observed with the TDWR (5.35-cm wavelength) at 6 min intervals. Interlaced with these sectors are sectors offset in time by 20 s but are not plotted because they contain similar information. Prior to the start (at 2139 CDT) there is no evidence of returns from the fireworks (within the circle). The peak of reflectivity in each circle after 2139 CDT is from the fireworks. These peaks are 15 dBZ larger than the background reflectivity of 5 to 6 dBZ. The color bar depicts categories of reflectivity in dBZ.

relate these to the magnitude of Z in the Z–D (diameter) relation. Recall that the maximum number of stars we counted is 325. The actual number can be a few to about 1,000 (if three of more bursts overlap). Assume that 300 stars fill the largest resolution volume (WSR-88D; Table 2). This realistic high number produces the equivalent concentration[1] $n = 2 \times 10^{-4}$ m^{-3}, which is convenient for scaling to other concentrations.

For Rayleigh scattering spheres of equal size, the equivalent reflectivity factor is [Doviak and Zrnić 2006, their Eq. (4.33)]

$$Z_e = D^6 |K_m|^2 / |K_w|^2 n = 0.35 D^6 n, \qquad (2)$$

[1] The stars can be located in a small part of the volume and the Z would be almost the same as if uniformly spaced.

where the dielectric factor of water $|K_w|^2 = 0.93$, and $|K_m|^2 = 0.33$ is the dielectric factor of the stars (see the appendix); Z_e is in mm^6 m^{-3}, D is in mm, and n is in m^{-3}. Assuming $n = 2 \times 10^{-4}$ m^{-3} we have plotted the corresponding Z_e in Fig. 12 for Rayleigh [Eq. (2)] and Mie scattering (at the three wavelengths; see appendix). The graphs suggest that the reflectivities of 15 to 22 dBZ may come from 8- to 12-mm scatterers; 2 times larger/smaller concentrations would increase/decrease these reflectivities by 3 dB. The data in Fig. 11 imply that it is unlikely the maximum concentrations were smaller, if anything they were larger. For example, 900 stars in the resolution volume increases Z to 27 dBZ exceeding most data in Fig. 11.

A fair comparison between the Z from the WSR-88D and the TDWR we make for the heights 135 and 140 m (Fig. 11, Fig. 3, Table 2). The beam centers are within 5 m of each other and the lateral dimensions of the beams are similar (90 and 110 m). The depths of the resolution volume are about 235 m for the WSR-88D and 150 m for the TDWR. Therefore, the resolution volume sizes of the two are almost equal; the WSR-88D's is 5% larger than the TDWR's. The measured Zs do not overlap and the difference of the averages is 6.5 dB (Fig. 11). 18 mm stars can cause this difference (Fig. 12) but their number would have to be 10 times smaller to match the reflectivities; that is still a realistic possibility. If refractivity were the main contributor, the difference would be 9.7 dB (ratio of wavelength to the 11/3 power and in dB; Rogers and Brown 1997). If stars of 10 mm

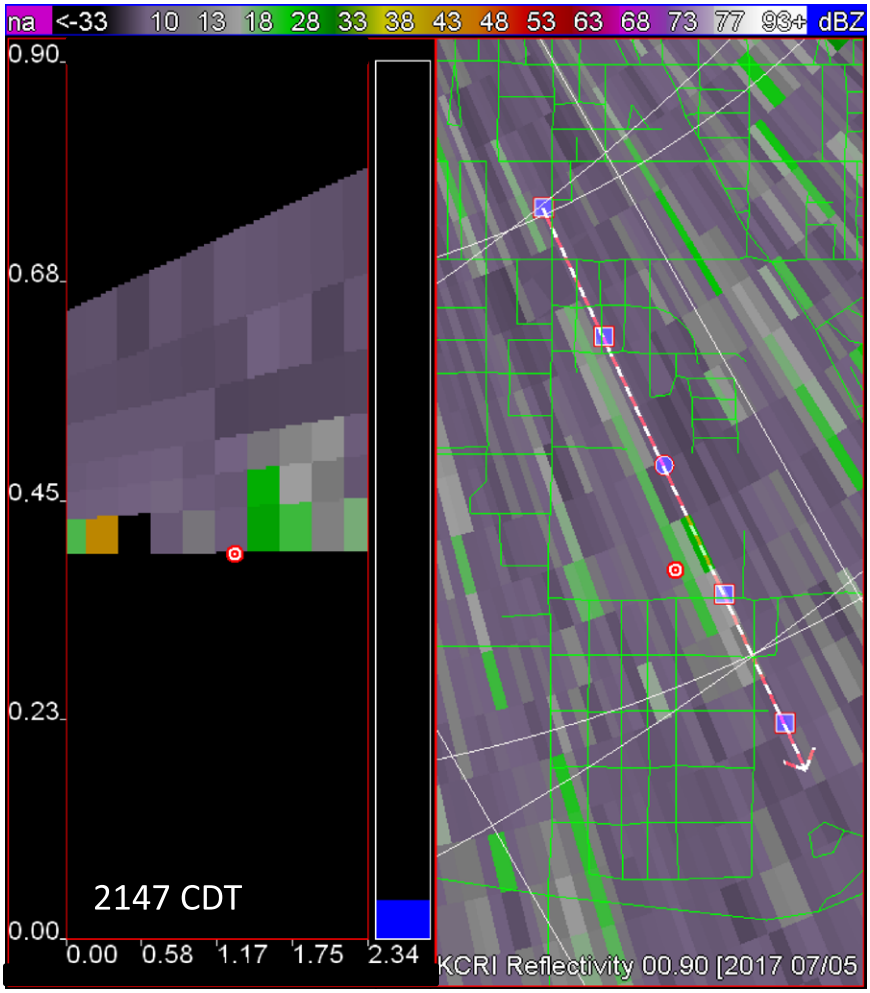

Fig. 10. (left) Vertical (reconstructed RHI) and (right) conical (PPI) cross sections of the reflectivity field from the WSR-88D (Norman) radar at 2147 CDT. The location of the vertical cross section (RHI) is drawn with a dashed line in the PPI plot. Note that the enhanced Z in the two bottom radials of the RHI could not be caused by the same burst because the two radials of data are separated in time by over three minutes. This is much longer than the burst's several seconds lifetime. The categories of reflectivity in dBZ are depicted on the color bar. The distances are in kilometers.

size are present together with refractivity variation and the ratio of stars contribution to refractivity contribution at 5 cm wavelength is 10/6 the difference $Z(10) - Z(5)$ would be about 6 dB in agreement with the value at 135–140 m above ground (Fig. 11). Although plausible, this agreement might be fortuitous because, there are only two points at λ = 10 cm, the observations are not coincident in time, other contributors such as rockets carrying shells may be present, and there is significant uncertainty in the values of the dielectric constants used for computing Z in Fig. 12.

For stars 10 to 15 mm size, the Z_es at the 5- and 10-cm wavelengths are clearly separated from the Z_e at the 3-cm wavelength (Fig. 12). For these diameters, we call the scatterers sensed by the 5-cm wavelength radar "quasi Rayleigh" as they depart by at most 3 dB from the Rayleigh limit. At the assumed concentration ($n = 2 \times 10^{-4}$ m^{-3}) the number of stars in the resolution volumes of the WSR-88D, TDWR, and XERES would be 300, 285, and 5.

The spread of Z and the maximum values measured by XERES are the largest of the three (Fig. 11). XERES has at least 10 times more data points at each elevation and its resolution volume is much smaller (see beam cross sections in Fig. 4 and Table 2). It may capture all the stars at the early stage while their expansion sphere is small and inside the volume. As the sphere expands, the number of captured stars (and associated Z_e) depends on which part of the sphere is contained within the resolution volume. During the early stage there can be 100+ stars in the resolution volume and if these are up to 15 mm the Z_e could increase to 40 dBZ; the increase is $10\log(n_a/n)$, where n_a is the actual concentration. This would shift the purple curve in Fig. 12 by about 20 dB and match the maximum observed (Fig. 11). Such Mie scattering stars can

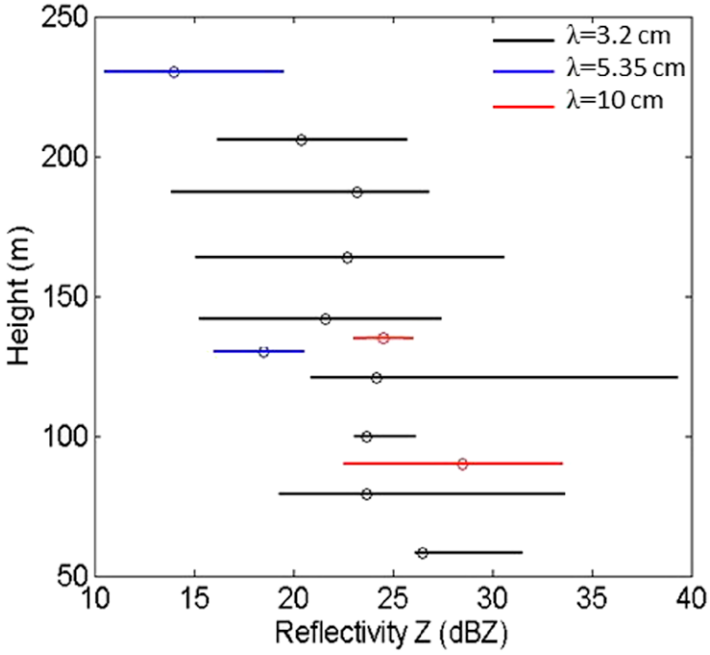

Fig. 11. Range of the peak reflectivity values measured by the three radars in Norman (XERES, 3.2-cm; TDWR 5.35-cm, and WSR-88D, 10-cm wavelength) at indicated heights of the beam centers above the launch site. Circles indicate average values.

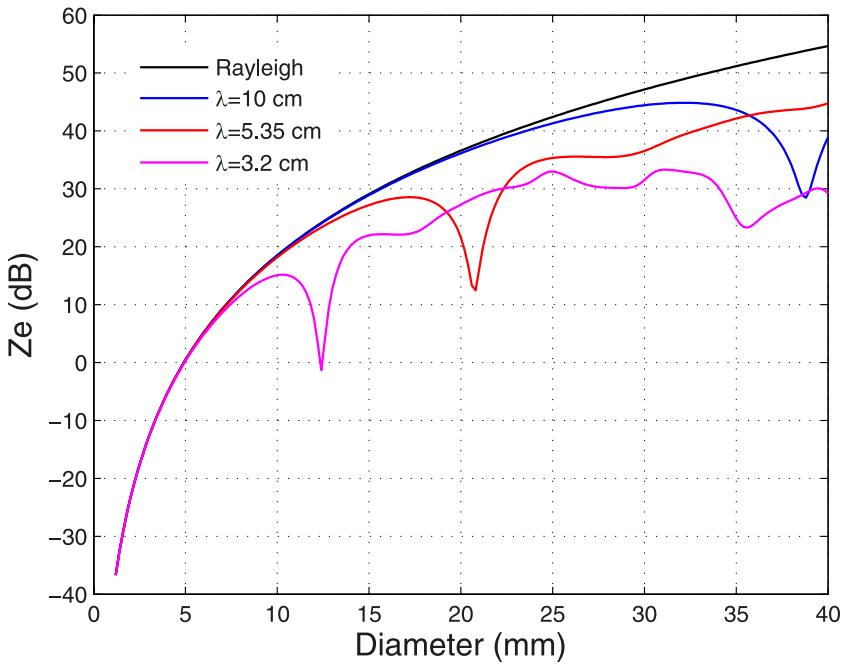

Fig. 12. Reflectivities vs diameter of spherical scatterers with dielectric properties of fireworks. The legend indicates the wavelengths and the Rayleigh curve. The Rayleigh law roughly holds at diameters where the Rayleigh curve is within 1 dB of the curves from the Mie solutions. The concentration $n = 2 \times 10^{-4}$ m^{-3}.

explain the observations but larger scatterers like rockets with shells, shell pieces, and clumps of stars can as well. For example, a 20 cm shell full of stars would produce the reflectivity Z of about 30 dBZ if it is located at beam center (6 dB less if it is at the edge of the beam). The rocket caring this shell would add few more dBs to the total. Although the maximum reflectivity clearly stands out, the dynamic range of Z from fireworks overlaps that from biota. Birds and/or bats cause the strong point reflectivities sensed by the WSR-88D outside the fireworks region.

The high (33 to 39 dBZ) Zs from fireworks are much larger than the 20 dBZ in smoke from wildfires (Melnikov et al. 2008) and apartment fires (Jones et al. 2009). The scatterers in these plumes are millimeter-size oriented particles, which produce spread of Z_{DR} between −2 and 7.9 dB similar to the spread from fireworks (on the WSR-88Ds the magnitudes of differential reflectivity are truncated at 7.9 dB).

Fireworks in Fort Worth

The city of Fort Worth has the largest fireworks display in northern Texas. Its Fourth of July celebration is held at Panther Island Park. The 2018 show lasted about 30 minutes and the location of the launch was at a distance of 20.5 km from the WSR-88D (designated as KFWS).

The volume update time was 5 min and fireworks were detected in all five consecutive scans at the 0.5° elevation. The longest extent of fireworks reflectivity in range is 2.5 km, and in azimuth, it is 2.5° or 900 m (Fig. 13). We deduce that a few closely spaced bursts caused this patch, because it is longer than the maximum extent of any single burst. A 3-ft shell (maximum in commercial fireworks) would create a "bloom" up to 500 m across (Siegel 2016).

The Doppler velocities in the region close to the fireworks are mainly between 10 and 15 m s^{-1}, and some are even higher. There is a decrease to about 5 m s^{-1} at ranges closer to the radar, and velocities are negative (i.e., toward the radar) along a 1-km segment in the middle radial. Both features indicate divergence that did not originate from a single burst. Furthermore, it confirms that the stars are the overwhelming contributors to the returns compared to refractivity.

The σ_v (Fig. 13) in the fireworks is between 8 and 12 m s^{-1} and the background values are 4 to 5 m s^{-1}. The values are significantly larger than the 2 to 3 m s^{-1} measured with the Norman WSR-88D, mainly because Fort Worth radar's beam cross section at the measurement location

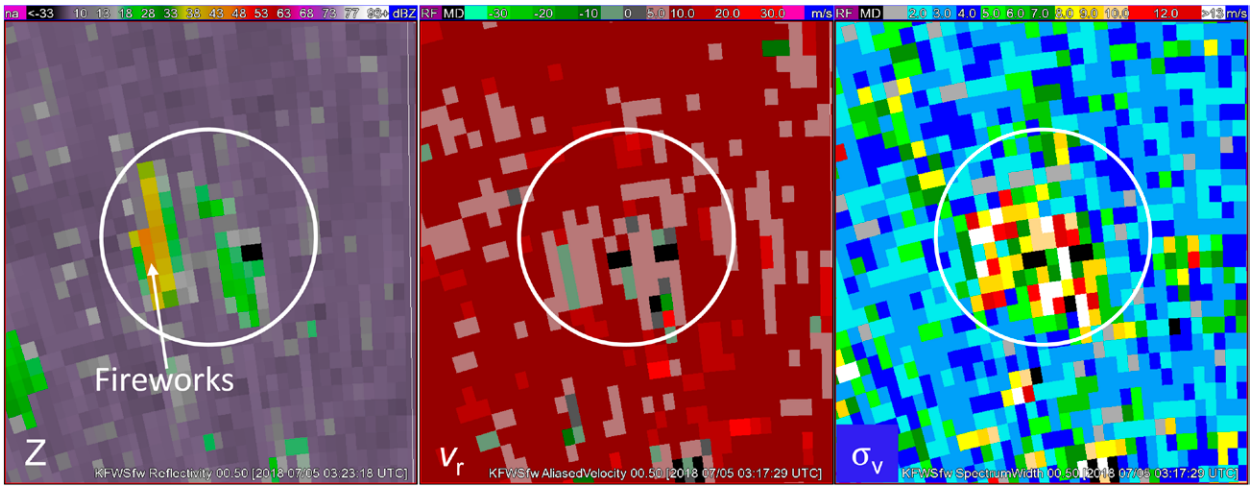

Fig. 13. Fields of reflectivity Z (in dBZ), Doppler velocity v_r (in m s^{-1}), and Doppler spectrum width σ_v (in m s^{-1}). The diameter of the white circle is 3.5 km. The data are from the operational WSR-88D over the Dallas–Fort Worth metropolitan area. The arrow points to the patch caused by the fireworks. The patch to the right is caused by reflections off buildings. Time and date are at 2123 CDT 4 Jul 2018. The pixel spacing in range is 250 m and in azimuth it is 0.5° (about 175 m in the middle of the circle). The elevation angle is 0.5° and the color bars indicate categories of Z in dBZ, and v_r and σ_v both in m s^{-1}.

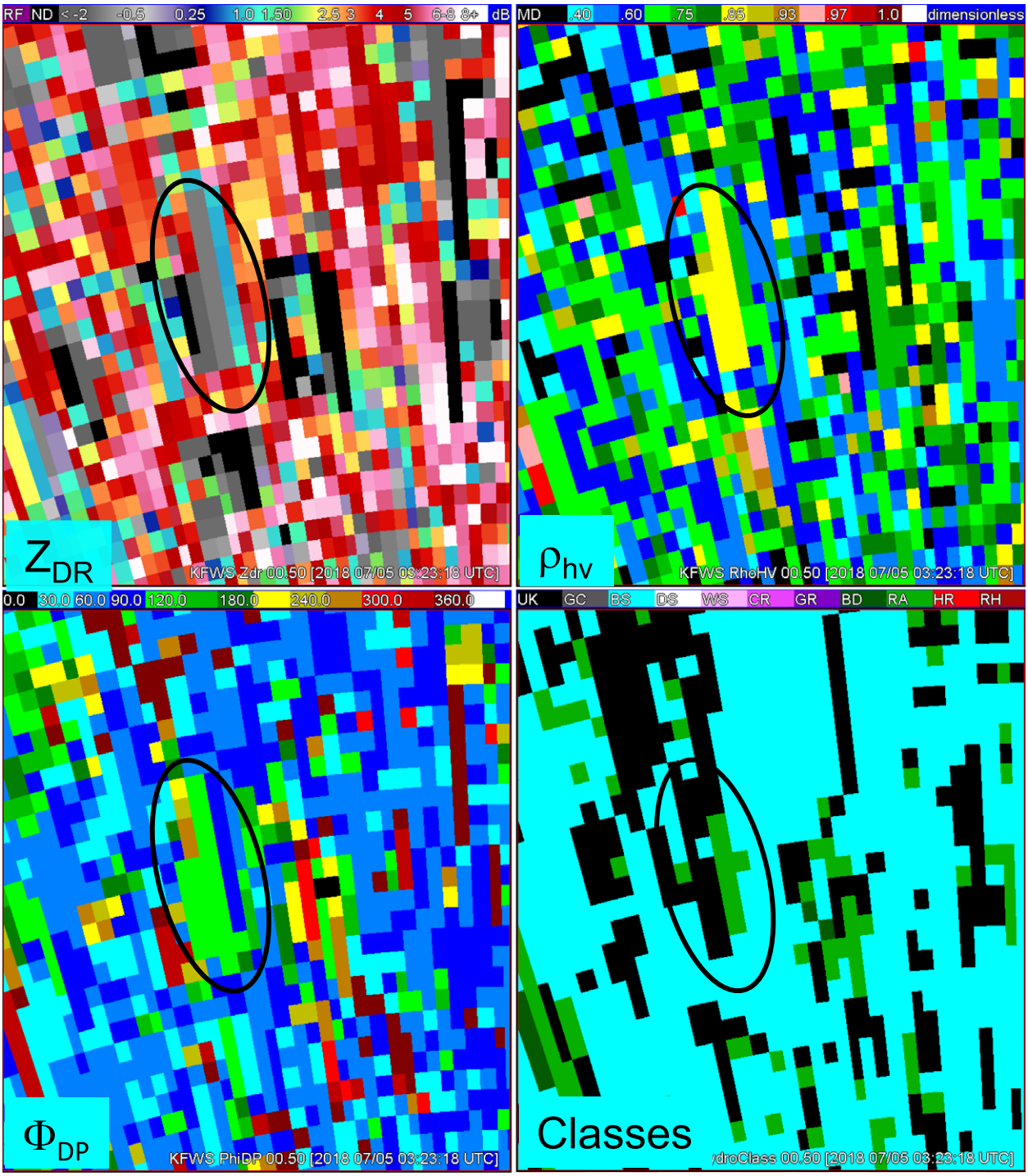

Fig. 14. As in Fig. 13, but the fields of differential reflectivity Z_{DR}, correlation coefficient ρ_{hv}, differential phase Φ_{DP}, and results of classification are plotted. The displayed differential phase Φ_{DP} (in degrees) contains the system phase Φ_{DP} (system), which is 60° and the backscatter differential phase δ. The ellipse encloses data from the fireworks. Colors on the bars above each field indicate values of the corresponding variable. Class categories above the field of classes are as follows: UK—unknown; GC—ground clutter; BS—biological; DS—dry snow; WS—wet snow; CR—crystals; GR—graupel; BD—big drops; RA—rain; RH—heavy rain; HR—hail rain mixture.

is 16 times larger. Therefore, it illuminates a much larger space containing a proportionately bigger variety of scatterers and their velocities.

The Z_{DR} is persistently negative (even smaller than −4 dB) excluding contribution by refractivity. The ρ_{hv} of about 0.85 is in the range for nonmeteorological scatterers but stands out from the background. Both Z_{DR} and ρ_{hv} are within the ranges for giant (>5 cm) hail (Ryzhkov and Zrnić 2019). The differential phase from the location of maximum Z is about 146°. It consists of the system differential phase of 60° and δ = ~86° of the "stars." Balakrishnan and Zrnić (1990) and Mirković (2015) computed comparable δ for 5 to 6 cm hailstones.

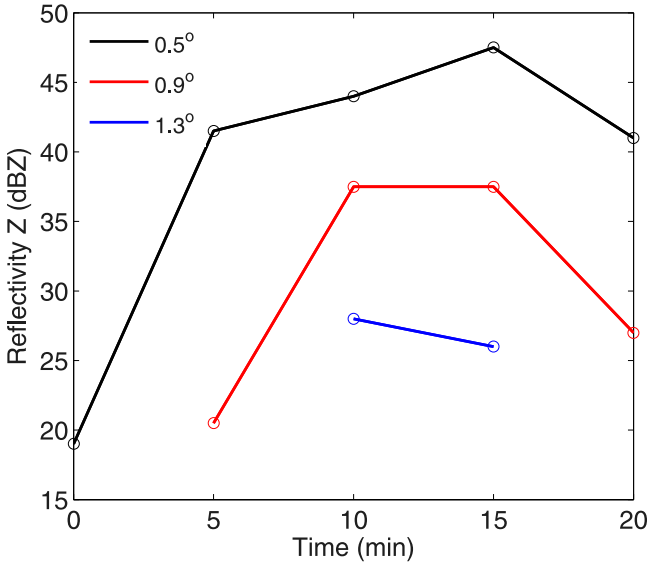

Fig. 15. Variations in time of the peak reflectivities at three elevation angles. Data are from the Fort Worth fireworks as in Figs. 13 and 14.

In the fourth panel of Fig. 14 are the results of return classification (Park et al. 2009). The light blue areas indicate biota, which in this case is nocturnal insects and possibly some birds and/or bats. The green areas corresponding to rain are misclassifications because the polarimetric variables from rain overlap significantly with the ones from biota and the algorithm has not been adjusted to make the distinction. The fireworks' returns are mainly in the unknown (black areas) class, about 25% are misclassified as rain, and ~15% are in the biological class. In other scans the fireworks are similarly classified. The algorithm identifies most fireworks as nonmeteorological scatterers enabling some elimination from precipitation.

The profiles of the peak Z in time and elevation (determined manually) show four consecutive values bigger than 40 dBZ at the 0.5° elevation (Fig. 15). The maximum is 47.5 dBZ, which, if it were rain, it would correspond to about 34 mm h^{-1}. At this elevation, the beam center over the launch site is 254 m above ground, which is slightly more than the 230 m altitude of the beam center in the highest of the Norman scans (Fig. 11). Obviously the Fort Worth fireworks are produced by significantly larger and more powerful shells. The reflectivities are, on average, larger by about 20 dB than reflectivities of the Norman fireworks (Fig. 11). The consistent decrease of Z with height (elevation angle) is likely caused by partial beam filling.

The Z_{DR}, ρ_{hv}, and δ are very variable, and in Table 3 we list the averages at the three elevation scans and similar averages but at two elevations scans in case of the Norman fireworks recorded by the WSR-88D. We took averages of the values measured at the peak of reflectivity at each scan presumably because these are most representative of the fireworks' return.

Both the spread of average Z_{DR} (−2.7 to 3.6 dB) and overall spread (−7.6 to 7.9 dB) are significantly larger in the Fort Worth fireworks than the Norman ones, (0.1 to 2.6 dB) and (−1.4 to 7.9 dB). Similarly, the spread of the average backscatter differential phase (−26° to 44°) from the Fort Worth fireworks and the overall dispersion (−150° to 86°) significantly exceed the (12° to 14°) and (−17° to 48°) values observed in the Norman fireworks. This suggests there could be a fundamental difference in the scattering characteristics of the stars.

Table 3. Average values and spread (in parentheses indicated with "to"; the comma separates two single observations) of differential reflectivity and backscatter differential phase obtained by the WSR-88D radars in Fort Worth and Norman.

Elevation (°)	Fort Worth Z_{DR} (dB)	Norman Z_{DR} (dB)	Fort Worth δ (°)	Norman δ (°)
0.5	−2.7 (−7.6 to 2.6)	2.6 (−1.4 to 7.9)	44 (−20 to 86)	12 (−17 to 48)
0.9	3.6 (−0.7 to 7.9)	0.1 (−0.7, 0.9)	−26 (−150 to 57)	14 (1, 28)
1.3	1.9 (0.4, 3.5)		29 (2, 56)	

It is likely that sizes of many stars in the Fort Worth fireworks are very large and exceed the Rayleigh limit. Also, because the beam cross section is about 16 times larger a bigger part of the burst is captured by the radar in Fort Worth than the radars in Norman. Finally, the rockets and shells in Fort Worth are larger than in Norman, and therefore have larger reflectivities.

The stars burn at temperatures lower than about 1,800°C (Shimizu 2006). This is not sufficient to ionize gas and cause reflection. Also the flames reflect orders of magnitude less power than the bodies of the stars. This implies the dominant scatterers in the Fort Worth case are the stars and/or rockets carrying shells and either overwhelms the contribution (if any) by refractivity. Because the span of Z_{DR} and backscatter differential phase values are large, we conclude that the objects responsible for Mie scattering are not spherical and maintain orientation in fall. The stars before the burning stage may be cylinders, rectangular parallelepipeds, or spheres. Burning could change their shape and in fall they would acquire an orientation. At the same orientation but depending on size, these stars would produce positive or negative Z_{DR} and large variation of backscatter differential phase. This is what we observe, but with no knowledge of the refractive index and orientation, it is not possible to be more quantitative.

Discussion

We have presented observations of Norman fireworks made on 4 July 2017 with WSR-88D weather radar (10-cm wavelength), TDWR (5.35-cm wavelength), and the NSSL XERES research mobile radar (3.2-cm wavelength). Simultaneous video recording of the event helped relate the physical properties of these fireworks to radar measurement. Typical heights of the bursts are between 100 and 200 m above ground, and the highest burst occurred at 270 m. Most burst diameters are 100 to 150 m but few exceeded 200 m. The individual bursts last from 1 to 6 s and the terminal velocities of stars in the majority of symmetric bursts are 14 to 16 m s^{-1}. The largest terminal velocities are about 22 m s^{-1}, which is in the range of large hail.

On radars' displays, the burst appears as a patch of enhanced reflectivity above the launch site. The patch persists over time, although its morphology evolves. Based on video recordings and radar scanning patterns, we conclude that scans separated by 7 s are unlikely to capture the reflections off the same burst. Rather, the continuous sequence of bursts maps into time continuity of reflectivity peaks. Before the start of fireworks and after the end, there are no detections. Therefore, capturing the temporal change of the Z field is crucial for detecting the onset of bursts. This requires scanning most frequently at the lowest elevation, which is possible with agile beam phased array weather radars (Torres et al. 2016).

The range of reflectivities is between 10 and 39 dBZ. The averages are from 15 to 26 dBZ, and decrease systematically with height. This is caused by partial beam filling as fewer stars are intercepted at higher altitudes. The stars are most likely Rayleigh backscatterers (small compared to the wavelength) at the 10-cm wavelength and "quasi Rayleigh" at the 5-cm wavelength. This we deduced by comparing reflectivities at the two wavelengths with results from a Mie scattering model.

The resolution of the 3-cm wavelength radar is 63.6 times finer than the resolution of the 10-cm wavelength radar. Therefore, precise comparison of reflectivities is not possible hence the type of scattering at the 3-cm wavelength is hard to determine. The observed values overlap the reflectivities measured at the two longer wavelengths. Comparison with the Mie model indicates that stars with diameters up to 7-mm are in the Rayleigh scattering regime while the larger ones are in the Mie regime.

Detections in the Norman case are much easier at the 3 and 5-cm wavelengths because the reflectivity of bursts stands out in the bland background of 5 to 15 dBZ values. At the 10-cm wavelength, the background values are similar, but additionally numerous speckles of reflectivities larger than 20 dBZ are imbedded. These are caused by big scatterers (birds

and/or bats) reflecting in the Rayleigh regime at λ = 10 cm and the Mie regime at the 5- and 3-cm wavelengths. Therefore, the reflectivity of this biota is much larger at the 10-cm wavelength and similar to the reflectivity of the fireworks. Only the sudden appearance of the bursts' reflectivity and its persistence (15 min) at the same patch (few range locations and 1 to 3 adjacent azimuths) alerts observers that something other than biota is present. The polarimetric variables from fireworks offer no clue because they overlap heavily with the ones from nonmeteorological scatterers. Although the maximum reflectivities clearly stand out, the dynamic range of Z from fireworks overlaps the one of biota.

Radar returns off the Fort Worth fireworks differ significantly from the ones in Norman. The planar size of the enhanced reflectivity patch extends 800 m across the beam and 2,250 m along range, in contrast to the 200 m lateral and 400 m along range patch observed with the TDWR in Norman. The peak reflectivities of the Fort Worth fireworks are 10 dB larger, and the maximum is 47.5 dBZ. The spectrum widths are over 8 m s^{-1}, whereas in Norman, the largest is 4 m s^{-1}. This is because the beam in Fort Worth illuminates 16 times larger space than the beam of the WSR-88D in Norman; therefore, it captures bigger parts of bursts and consequently a wider spread of stars' Doppler velocities. Radial divergence is observed in both Norman and Fort Worth fireworks. The values of the polarimetric variables in the Norman fireworks are subdued and blend with the ones from biota. In the Fort Worth case, the backscatter differential phase has a large spread, and the differential reflectivity exhibits significant negative values. Both are in the range of giant hail. The correlation coefficient's values between 0.85 and 0.89 stand out compared to the biota. These polarimetric variables indicate that the dominantly contributing stars observed in Fort Worth (10-cm wavelength), are oriented Mie scatterers with sizes of several centimeters. Clearly, there are fundamental differences between the smaller fireworks in Norman and the Fort Worth ones, which have larger shells, bigger bursts, and greater number.

Unlike smoke plumes generated by fires, the fireworks produce small amount of visible smoke. Moreover, we have no evidence of lightweight mm to cm size particles, which are common in ordinary fires. This excludes the possibility suggested by Erkelens et al. (1999) that coherent scattering by the variation of particle (smoke) concentration in range is present. Whether stars create sufficient variation of refractivity to be detectable is an open question. In clear cases (i.e., large negative differential reflectivity, or diverging Doppler velocities) dominance of stars' bodies is obvious. Otherwise, we have no evidence either way. Simultaneous observations at two frequencies combined with polarimetric spectral analysis may resolve this issue.

The stars reflect sufficient energy, which weather radars can detect. By analogy, we expect similar detection of explosions. Pinpointing locations would be useful to first responders, or air quality forecasters. A benefit of fireworks recognition in weather radar data are that it can prevent contamination of precipitation accumulations.

Fireworks are a common highlight in national celebrations around the world. People look forward to enjoying these shows. Municipalities and venues produce shows of spectacular size and artistry to please their audiences and attract visitors. We propose a different way to experience fireworks. It is by observing their images on displays of the National Weather Service WSR-88D data. These can tell the spatial extent of the spectacle and the heights of bursts. Moreover, it is possible to roughly infer the size of significant stars, and components of their velocity. The color variety of the polarimetric variables on radar displays is one thing common with visual observations. Using smart phones, the public can observe radar images and the real thing at the same time.

Acknowledgments. We thank Mr. Matt Hendren, park superintendent city of Norman, for the information about Norman fireworks location and size. Ms. L. Richardson of Radar Operations Center determined the initial differential phase of the WSR-88D in Norman and verified timing, and Mr. R. Lee gave us the data. Mr. J. Murnan helped with the video equipment and synchronized its timing. Ms. A. Murphy's and A. Ryzhkov's suggestions improved comprehension and clarity. Dj. Mirković informed us about backscattering of large objects. The questions and suggestions by three anonymous reviewers prompted us to create and examine the model of fireworks' stars and consequently revise parts of conclusions. Partial funding for this work was paid by the U.S. Department of Homeland Security Science and Technology and Federal Emergency Management Agency. V. Melnikov and P. Zhang were supported by NOAA/Office of Oceanic and Atmospheric Research under NOAA-University of Oklahoma Cooperative Agreement NA11OAR4320072.

Appendix: Properties of fireworks

The typical filling material consists of powders: 75% potassium nitrate, 15% charcoal, and 10% sulfur. The density of this composition is about 0.9 g cm^{-3} (Kayaku Japan Co.). The complex relative dielectric constant ε of the mixture is $5.06 + j0.27$ and the corresponding dielectric factor $|K_m|^2 = 0.33$. The ε is computed according to the formula (Nelson 2005) $\varepsilon^{1/2} = \alpha_1\varepsilon_1^{1/2} + \alpha_2\varepsilon_2^{1/2} + \alpha_3\varepsilon_3^{1/2}$, where α_is are the volume fractions (contribution by air is neglected). The dielectric constants of potassium nitrate (NKO_3), $\varepsilon_1 = 5$ (at 60 MHz; Golio 2001) and we assume it is the same at microwave frequencies. Of charcoal powder (carbon black) $\varepsilon_2 = 6 + j2$ (at frequencies 3 to 9 GHz; Hotta et al. 2011) and of sulfur $\varepsilon_3 = 4$ (average; Golio 2001). The equivalent reflectivity factor of the stars we compute from the formula (Doviak and Zrnić 2006), $Z_e = n\sigma\lambda^4/(\pi^5|K_w|^2)$, where σ (mm^2) is the backscattering cross section of the star, n is the number of stars per m^3, $|K_w|^2 = 0.93$, and λ is in mm. We assume spherical shape and equal sizes of all stars and compute the σ according to the Mie formula (Bohren and Huffman 1998). We choose $n = 2 \times 10^{-4}$ m^{-3} and then computed the Z_e (Fig. 12). For comparisons and reference, we can define the Rayleigh limit (diameter D_r) up to which the Rayleigh and Mie cross sections (or reflectivities) differ by at most 1 dB. The sizes are the following: at $\lambda = 10$ cm, $D_r = 23$ mm; at $\lambda = 5.35$ cm, $D_r = 12.2$ mm, and at $\lambda = 3.2$ cm, $D_r = 7.4$ mm.

References

Balakrishnan, N., and D. S. Zrnić, 1990: Estimation of rain and hail rates in mixed-phase precipitation. *J. Atmos. Sci.*, **47**, 565–583, https://doi.org/10.1175/1520-0469(1990)047<0565:EORAHR>2.0.CO;2.

Banta, R. M., L. D. Oliver, E. T. Holloway, R. A. Kropfli, B. W. Bartram, R. E. Cupp, and M. J. Post, 1992: Smoke-column observations from two forest fires using Doppler lidar and Doppler radar. *J. Appl. Meteor.*, **31**, 1328–1349, https://doi.org/10.1175/1520-0450(1992)031<1328:SCOFTF>2.0.CO;2.

Bohren, G. F., and D. R. Huffman, 1998: *Absorption and Scattering of Light by Small Particles.* Wiley, 530 pp.

Chilson, P., and Coauthors, 2012: Partly cloudy with a chance of migration. *Bull. Amer. Meteor. Soc.*, **93**, 669–686, https://doi.org/10.1175/BAMS-D-11-00099.1.

Doviak, R., and D. S. Zrnić, 2006: *Doppler Radar and Weather Observations.* 2nd ed. Dover Publications, 592 pp.

Erkelens, J. S., V. K. C. Venema, and H. W. J. Russchenberg, 1999: Coherent particle scatter in smoke and cumulus clouds. *Proc. Int. Geoscience and Remote Sensing Symp.*, Hamburg, Germany, IEEE, 687–689, https://doi.org/10.1109/IGARSS.1999.773606.

Golio, M., Ed., 2001: *The RF and Microwave Handbook.* CRC Press, 1376 pp.

Heymsfield, A., M. Szakall, A. Jost, I. Giammanco, and R. Wright, 2018: A comprehensive observational study of graupel and hail terminal velocity, mass flux, and kinetic energy. *J. Atmos. Sci.*, **75**, 3861–3885, https://doi.org/10.1175/JAS-D-18-0035.1.

Hotta, M., M. Hayashi, M. T. Lanagan, D. K. Agrawal, and K. Nagata, 2011: Complex permittivity of graphite, carbon black and coal powders in the ranges of X-band frequencies (8.2 to 12.4 GHz) and between 1 and 10 GHz. *ISIJ Int.*, **51**, 1766–1772, https://doi.org/10.2355/isijinternational.51.1766.

Hubbert, J. C., J. W. Wilson, T. M. Weckwerth, S. M. Ellis, M. Dixon, and E. Loew, 2018: S-Pol's polarimetric data reveal detailed storm features and insect behavior. *Bull. Amer. Meteor. Soc.*, **99**, 2045–2060, https://doi.org/10.1175/BAMS-D-17-0317.1.

Hufford, G. L., H. L. Kelley, W. Sparkman, and R. K. Moore, 1998: Use of real-time multisatellite and radar data to support forest fire management. *Wea. Forecasting*, **13**, 592–605, https://doi.org/10.1175/1520-0434(1998)013<0592:UORTMA>2.0.CO;2.

Jones, T. A., S. A. Christopher, and W. Petersen, 2009: Dual-polarization radar characteristics of an apartment fire. *J. Atmos. Oceanic Technol.*, **26**, 2257–2269, https://doi.org/10.1175/2009JTECHA1290.1.

Marzano, F. S., E. Picciotti, M. Montopoli, and G. Vulpiani, 2013: Inside volcanic clouds: Remote sensing of ash plumes using microwave weather radars. *Bull. Amer. Meteor. Soc.*, **94**, 1567–1586, https://doi.org/10.1175/BAMS-D-11-00160.1.

Melnikov, V. M., D. S. Zrnić, R. M. Rabin, and P. Zhang, 2008: Radar polarimetric signatures of fire plumes in Oklahoma. *Geophys. Res. Lett.*, **35**, L14815, https://doi.org/10.1029/2008GL034311.

Milinskiy, A. Y., and A. A. Antonov, 2015: Dielectric properties of a potassium nitrate–ammonium nitrate system. *St. Petersburg Polytech. Univ. J. Phys. Math.*, **1**, 239–244, https://doi.org/10.1016/j.spjpm.2015.11.005.

Mirković, Dj., 2015: Computational electromagnetics applied to scattering observed by polarimetric weather radar. Ph.D. dissertation, University of Oklahoma, 241 pp.

Nelson, S. O., 2005: Density-permittivity relationships for powdered and granular materials. *IEEE Trans. Instrum. Meas.*, **54**, 2033–2040, https://doi.org/10.1109/TIM.2005.853346.

Park, H., A. Ryzhkov, D. Zrnić, and K.-E. Kim, 2009: The hydrometeor classification algorithm for the polarimetric WSR-88D: Description and application to an MCS. *Wea. Forecasting*, **24**, 730–748, https://doi.org/10.1175/2008WAF2222205.1.

Rauber, R. M., and S. W. Nesbitt, 2018: *Radar Meteorology: A First Course.* John Wiley and Sons, 461 pp.

Rogers, R. R., and W. O. Brown, 1997: Radar observations of a major industrial fire. *Bull. Amer. Meteor. Soc.*, **78**, 803–814, https://doi.org/10.1175/1520-0477(1997)078<0803:ROOAMI>2.0.CO;2.

Ryzhkov, A. V., and D. S. Zrnić, 2019: *Radar Polarimetry for Weather Observations.* Springer 486 pp.

——, T. J. Schuur, D. W. Burgess, and D. S. Zrnić, 2005: Polarimetric tornado detection. *J. Appl. Meteor.*, **44**, 557–570, https://doi.org/10.1175/JAM2235.1.

——, M. Diederich, P. Zhang, and C. Simmer, 2014: Utilization of specific attenuation for rainfall estimation, mitigation of partial beam blockage, and radar networking. *J. Atmos. Oceanic Technol.*, **31**, 599–619, https://doi.org/10.1175/JTECH-D-13-00038.1.

Saraiva, E. A., R. V. Soares, A. C. Batista, H. Tertuliano, and A. M. Gomes, 2014: Monitoring forest fires and burnings with weather radar. *Advances in Forest Fire Research*, D. X. Viegas, Ed., Coimbra University Press, 1436–1443.

Shimizu, T., 2006: Manufacturing processes for firework compositions: Japanese fireworks. *Fireworks Principles and Practice*, R. Lancaster, Ed., Chemical Publishing, 371–440.

Siegel, E., 2016: The physics of fireworks. Forbes, www.forbes.com/sites/startswithabang/2016/07/01/the-physics-of-fireworks/#1e4a56ef1eee.

Stepanian, P. M., K. G. Horton, V. M. Melnikov, D. S. Zrnić, and S. A. Gauthreaux Jr., 2016: Dual-polarization radar products for biological applications. *Ecosphere*, **7**, e01539, https://doi.org/10.1002/ecs2.1539.

Torres, S., and Coauthors, 2016: Adaptive-weather-surveillance and multifunction capabilities of the National Weather Radar Testbed phased-array radar. *IEEE Proc.*, **104**, 660–672, https://doi.org/10.1109/JPROC.2015.2484288.

Weber, M., J. Y. N. Cho, J. S. Flavin, J. M. Herd, W. Benner, and G. Torok, 2007: The next-generation multi-mission U.S. surveillance radar network. *Bull. Amer. Meteor. Soc.*, **88**, 1739–1751, https://doi.org/10.1175/BAMS-88-11-1739.

Zrnić, D. S., 2003: Cost benefit analysis. National Severe Storms Laboratory Rep., 5 pp., www.nssl.noaa.gov/publications/wsr88d_reports/.

——, and A. V. Ryzhkov, 1998: Observations of insects and birds with a polarimetric radar. *IEEE Trans. Geosci. Remote Sens.*, **36**, 661–668, https://doi.org/10.1109/36.662746.

——, and Coauthors, 2007: Agile beam phased array radar for weather observations. *Bull. Amer. Meteor. Soc.*, **88**, 1753–1766, https://doi.org/10.1175/BAMS-88-11-1753.